CCS Chemistry

RESEARCH ARTICLE

Received: July 31, 2024 | Accepted: Nov. 26, 2024 | Published: Dec. 27, 2024

Defect-Rich Copper Electrocatalyst with Enhanced Acetylene Adsorption for Highly-Selective Ethylene Production at Industrial Current Densities

Zeliang Wu[1,2†], Tao Wang[3†], Qihui Guan[3], Dongfang Li[2], Yaojie Lei[2], Yong Chen[2], Wei Hong[3], Chang Wu[4], Shailendra Kumar Sharma[4], Jinqiang Zhang[2*], Shixia Chen[3*], Guoxiu Wang[2*] & Jun Wang[3*]

[1]School of Resources and Environment, Nanchang University, Nanchang, Jiangxi Province 330031, [2]Centre for Clean Energy Technology, School of Mathematical and Physical Sciences, Faculty of Science, University of Technology Sydney, Sydney, NSW 2007, [3]School of Chemistry and Chemical Engineering, Nanchang University, Nanchang, Jiangxi Province 330031, [4]Chemical and Process Engineering Department, University of Canterbury, Christchurch 8140

**Corresponding authors: jwang7@ncu.edu.cn; guoxiu.wang@uts.edu.au; shixiachen@ncu.edu.cn; jinqiang.zhang@uts.edu.au;* [†]Z. Wu and T. Wang contributed equally to this work.

Cite this: *CCS Chem.* **2024**, Just Published. DOI: 10.31635/ccschem.024.202404849

Electrochemical semihydrogenation of acetylene (C_2H_2) using renewable electricity offers a sustainable route for ethylene (C_2H_4) production. However, the development of this technique has been hindered by many challenges, such as competitive hydrogen evolution reactions (HERs) and overhydrogenation at high current densities, which will reduce the faradaic efficiency (FE) of C_2H_4 and negatively impact downstream processing. Herein, we develop defect-rich copper nanocubes (v-Cu NCs) as efficient electrocatalysts that facilitate C_2H_2 adsorption while suppressing HER and overhydrogenation. The superior semihydrogenation performances are verified by the high C_2H_4 FE of 98.3% at an ultrahigh current density of 0.7 A cm^{-2}. Remarkably, in a 25 cm^2 electrolyzer, v-Cu NCs deliver a record-high single-pass conversion of 97.5% for C_2H_2 and C_2H_4 selectivity of 97.4% at a cathode current of 1.6 A with a flow rate of 10 mL min^{-1}, operating stably for 50 h. In-situ Raman spectroscopy and theoretical calculations reveal that uniformly oriented Cu (100) planes and nitrogen vacancies generate strong C_2H_2 adsorption at copper sites, which facilitates hydrogenation kinetics and increases the energy barrier for overhydrogenation. This work offers valuable insights into the implementation of C_2H_2-to-C_2H_4 production and the development of efficient electrocatalysts for C_2H_2 semihydrogenation.

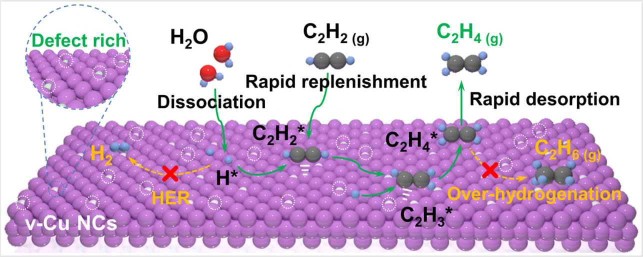

Keywords: electrochemical semihydrogenation, defect-rich, ethylene production, single-pass conversion rate, industrial current densities

Citation: *CCS Chem.* **2024**, Just Published. DOI: 10.31635/ccschem.024.202404849
Link to VoR: https://doi.org/10.31635/ccschem.024.202404849

Introduction

Ethylene (C_2H_4), a cornerstone of the global chemical industry, is predominantly produced through the cracking of petroleum and shale gas.[1–3] Dependence on fossil resources has stimulated the development of alternative production techniques, particularly the electrochemical semihydrogenation of acetylene (C_2H_2) to C_2H_4 (EHAE) using C_2H_2 from coal arc plasma.[4,5] Operating under ambient conditions and utilizing water as the proton source, EHAE offers a sustainable pathway powered by green and renewable electricity, while exhibiting high selectivity for C_2H_4 production.[2,6,7] However, the successful implementation of this method hinges on achieving a faradaic efficiency (FE) for C_2H_4 exceeding 85% at a current density of 0.2 A cm^{-2}, because of the substantial cost contribution of C_2H_2 to overall C_2H_4 production expenses (~75%).[2] Therefore, it is imperative to develop efficient electrocatalysts with enhanced electrocatalytic performance for EHAE processes.[2,8]

The developments in electrocatalysis technology and reactor designs, particularly in the use of nonprecious metal copper-based electrocatalysts, have substantially accelerated the industrialization of the EHAE process.[3,6,9] However, the low existing single-pass conversion (~16%) of C_2H_2 results in a substantial amount of unconverted C_2H_2 at the outlet, requiring multiple cycles for complete conversion and significantly escalating C_2H_4 production costs.[2,3] The enhancement of single-pass conversion of C_2H_2 is contingent upon the high C_2H_4 FE at industrial current densities.[10] However, most electrocatalysts currently fail to exhibit effective suppression of competitive hydrogen evolution reactions (HERs) at elevated current densities (>0.3 A cm^{-2}).[1,6,7,11–13] Moreover, the concurrent generation of overhydrogenated by-product ethane (C_2H_6) at the outlet (~2.5%) requires energy-intensive cryogenic distillation separation.[10,14–16] Therefore, it is crucial to suppress HER at the level of industrial current densities to enhance C_2H_2 single-pass conversion, at the same time avoiding the generation of C_2H_6 by-products.

Currently, the semihydrogenation of C_2H_2 is an efficient method for selectively removing trace amounts of C_2H_2 (1%) from crude C_2H_4, owing to its low required current density (<3 mA cm^{-2}). This process primarily focuses on minimizing the formation of undesired by-products such as C_2H_6 and 1,3-butadiene.[14] Thus, these electrocatalysts are intentionally designed to exhibit weak C_2H_2 adsorption to suppress overhydrogenation and C–C coupling reaction.[17–19] However, achieving high single-pass conversion rates for the production of C_2H_4 from pure C_2H_2 feedstock necessitates the utilization of high current densities (>0.3 A cm^{-2}).[2,3] Meanwhile, weak C_2H_2 adsorption also induces intensive competitive HER at high current densities, impeding efficient C_2H_2 to C_2H_4 semihydrogenation.[20] Theoretical calculations have revealed that the Cu (100) crystal facet exhibits strong affinities towards C_2H_2 and a higher barrier for HER, thereby possessing the potential to enhance single-pass conversion.[21] Moreover, the incorporation of defects in Cu-based electrocatalysts can further enhance C_2H_2 adsorption and increase the energy barrier for overhydrogenation, thereby reducing the formation of C_2H_6.[22] However, these strategies have not yet been experimentally validated in the EHAE process, and the underlying reaction mechanisms remain elusive.

Herein, we design and synthesize defect-rich copper nanocubes (v-Cu NCs) with primarily exposed Cu (100) facets as efficient EHAE electrocatalysts. As a result, v-Cu NCs exhibit a remarkable C_2H_4 FE of 98.3% at a high current density of 0.7 A cm^{-2} with pure C_2H_2 flow. The production rate for C_2H_4 reaches up to 17.69 mmol h^{-1} cm^{-2}, outperforming most reported electrocatalysts. In-situ Raman spectroscopy and density functional theory (DFT) calculations reveal that defect-rich Cu (100) facets enhance the adsorption of C_2H_2 and H*, thereby accelerating the reaction kinetics for semihydrogenation. Additionally, the presence of defects increases the energy barrier for overhydrogenation of $C_2H_4^*$ at the Cu sites to inhibit the formation of C_2H_6. Subsequently, v-Cu NCs showcase a 50-hour stability in a 25 cm^2 electrolyzer to continuously produce C_2H_4 with a single-pass C_2H_2 conversion rate of 97.5% and C_2H_4 selectivity of 97.4% at an ultrahigh current of 1.6 A and a flow rate of 10 mL min^{-1}.

Experimental Methods

Preparation of Cu_3N nanocubes

In a typical synthesis, 0.24 g of $Cu(NO_3)_2{\cdot}3H_2O$ was added to 10 mL of 1-octadecene, followed by the incorporation of 10 mL of oleylamine, stirred until a homogenous mixture was achieved. The solution was then subjected to vacuum heating at 130 °C for 30 min to ensure complete removal of water and oxygen, subsequently filled with ultrapure argon, and heated to 245 °C for 20 min. Notably, this thermal procession elicited a remarkable transition in the solution's coloration from a deep blue to a transparent yellow, culminating in a dark brown hue. Upon completion of the reaction, the product was naturally cooled down to room temperature, then dispersed in 30 mL of acetone, and subjected to centrifugal cleaning with hexane and acetone four times. The product obtained was then vacuum-dried at room temperature overnight.

Materials characterizations

The morphology and structure of the samples were characterized using X-ray powder diffraction (XRD, Bruker D8, Bruker Corporation, Germany), field emission scanning electron microscopy, and energy dispersive spectroscopy (EDS, Zeiss Supra 55VP, Carl Zeiss AG,

Citation: *CCS Chem.* **2024**, Just Published. DOI: 10.31635/ccschem.024.202404849
Link to VoR: https://doi.org/10.31635/ccschem.024.202404849

Germany), transmission electron micros,copy (TEM, F200; F200S, JEOL Ltd., Japan). High-resolution TEM (HRTEM) and EDS mapping images were analyzed using an F200S TEM operating at 200 kV. The chemical state was assessed through X-ray photoelectron spectroscopy (XPS, ESCALAB250Xi, Thermo Fisher Scientific, USA). X-ray absorption fine structure (XAFS) spectra were collected at the Australian National Synchrotron (Melbourne, Australia) and processed using ATHENA software.

Electrochemical measurements

Electrochemical experiments were performed on a CHI 660E workstation, enhanced with a CHI 680D high-current amplifier (CH Instruments, Inc., Shanghai, China). A three-electrode setup was utilized, featuring a prepared electrode as the working electrode, an Hg/HgO electrode as the reference, and Ni foam as the counter electrode. A FAB-PK-130 anion exchange membrane (AEM) effectively separated the cathode and anode compartments. C_2H_2 was introduced at a flow rate of 20 mL min^{-1} for semihydrogenation reactions with 1 M potassium hydroxide (KOH) electrolytic unless otherwise noted. Chronopotentiometry was used to study the electrochemical semihydrogenation of C_2H_2 at varying current densities over a consistent duration of 20 min, ensuring the determination of stable and accurate performance metrics for further analysis. Electrode potentials were recalibrated to the reversible hydrogen electrode (RHE) reference using the equation provided here:

$$E_{\mathrm{RHE}} = E_{\mathrm{Hg/HgO}} + 0.098\ \mathrm{V} + 0.059 \times \mathrm{pH}$$

Computational method

All the DFT calculations were performed using the Vienna Ab initio Simulation Package with the projector augmented wave method. The exchange-functional was treated using the generalized gradient approximation with the Perdew–Burke–Ernzerhof functional. The energy cutoff for the plane wave basis expansion was set to 400 eV. Partial occupancies of the Kohn–Sham orbitals were allowed using the Gaussian smearing method and a width of 0.2 eV. The structure of Cu (100) and v-Cu (100) were optimized using the k-point of $2 \times 2 \times 1$. The self-consistent calculations applied a convergence energy threshold of 10^{-5} eV, and the force convergency was set to 0.05 eV/Å. The transition state was located using the constrained optimization, where the force convergency was set to 0.05 eV/Å. The free energy corrections were considered at the temperature of 298.15 K, as follows:

$$\Delta G = \Delta E + \Delta G_{\mathrm{ZPE}} + \Delta U_G - T\Delta S$$

where ΔE, ΔG_{ZPE}, ΔU_G, and ΔS refer to the DFT calculated energy change, the correction from zero-point energy, the correction from inner energy, and the correction from entropy.

Results and Discussion

Morphological and structural characterizations

v-Cu NCs were synthesized through a two-step approach. In the first step, copper nitride nanocubes (Cu_3N NCs) were prepared by thermally decomposing divalent copper salts in an argon atmosphere using oleylamine as both a reducing agent and surface passivating ligand (Figure 1a).[23] The X-ray diffraction (XRD) patterns of Cu_3N NCs matched well with the standard Cu_3N sample (PDF# 47-1088) (Supporting Information Figure S1).[24] The as-synthesized Cu_3N NCs exhibited a uniform cubic morphology with an average size of approximately 25 nm, as shown in the TEM image (Figure 1b). The HRTEM image revealed that Cu_3N NCs possessed a cubic $Pm\bar{3}m$ structure with lattice spacings of 3.8 Å corresponding to the (100) plane (Figure 1c). The homogeneous distribution of copper and nitrogen within Cu_3N NCs was confirmed through energy-dispersive X-ray spectroscopy elemental mapping (Supporting Information Figure S2).[25,26] Furthermore, XAFS spectroscopy was employed to analyze the local atomic and electronic structures of Cu_3N NCs. The X-ray absorption near-edge structure spectrum of Cu_3N NCs displayed an edge energy positioned between that of Cu_2O and CuO, indicating a copper oxidation state ranging from +1 and +2 (Supporting Information Figure S3).[4,27] Extended X-ray absorption fine structure (EXAFS) analysis revealed the fine structure of Cu_3N NCs with two peaks located at 1.5 and 2.3 Å, corresponding to the Cu–N and Cu–Cu bonds, respectively (see Figure 1d).[27,28]

Cu_3N NCs were further subjected to in-situ electroreduction to synthesize the designed v-Cu NCs (Supporting Information Figure S4). Upon electrochemical reduction, the pseudo in-situ XRD patterns showed a complete conversion of pristine Cu_3N NCs into metallic Cu (Supporting Information Figure S5).[27] This transformation was also supported by postreaction XPS analysis. After the electroreduction, the Cu 2p orbital of v-Cu NCs shifted to lower energy levels, indicating electron transfers to Cu (Figure 1e and Supporting Information Figure S6a).[26,29] The position of the Cu LMM Auger peak shifted from 916.5 to 918.3 eV, indicating that partial Cu^+ species were reduced to Cu^0 species in Cu_3N NCs (Supporting Information Figure S6b).[3] Meanwhile, the N 1s signal significantly diminished, accompanied by the disappearance of Cu–N bonds (Supporting Information Figure S7).[29] Furthermore, the HRTEM image exhibited lattice fringes with an interplanar spacing of 1.8 Å that matched those of the (100) facet of Cu (Figure 1f).[30] The uniform cubic morphology was successfully retained by v-Cu NCs (Supporting Information Figure S8), indicating that the releasing of nitrogen species did not alter the overall morphology.[27] However, it is worth noting that a distinct

Citation: *CCS Chem.* **2024**, Just Published. DOI: 10.31635/ccschem.024.202404849
Link to VoR: https://doi.org/10.31635/ccschem.024.202404849

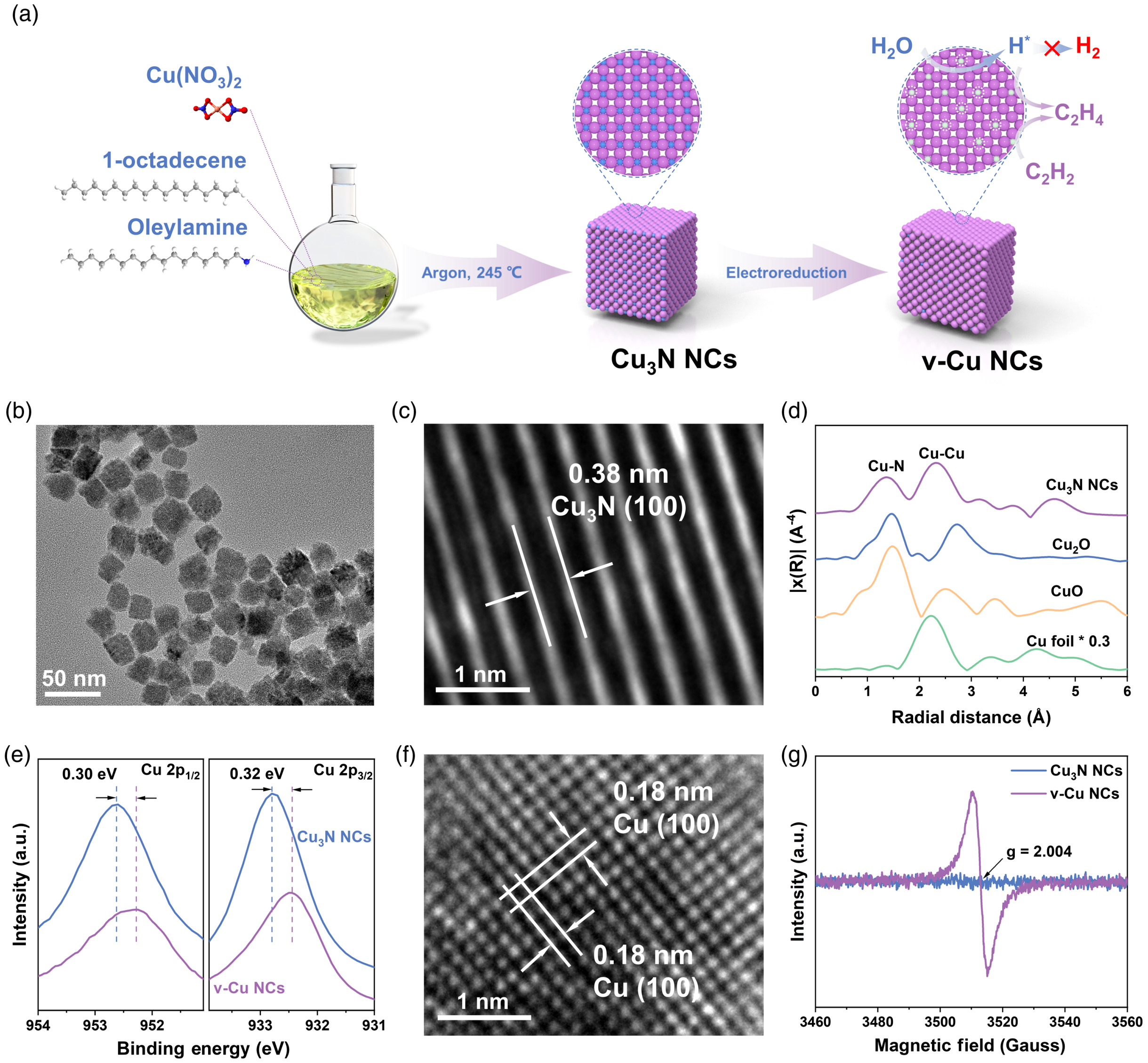

Figure 1 | *Morphology and chemical structural characterization. (a) Schematic illustration of the formation process. (b) TEM and (c) HRTEM images of Cu_3N NCs. (d) Cu K-edge FT-EXAFS spectra of Cu_3N NCs. (e) XPS spectra of Cu_3N NCs and v-Cu NCs in Cu 2p. (f) HRTEM image of v-Cu NCs. (g) EPR analysis of Cu_3N NCs and v-Cu NCs.*

signal at a *g*-value of 2.004 appeared in the electron paramagnetic resonance (EPR) spectrum after in-situ electroreduction, thereby confirming the generation of abundant nitrogen vacancies within v-Cu NCs (Figure 1g).[26,29,31]

Electrocatalytic acetylene semihydrogenation

We assessed the electrocatalytic performance of the EHAE process in a three-electrode flow cell (1 cm^2). In this setup, commercial nickel foam was employed as the counter electrode, and Hg/HgO electrodes served as reference electrodes. An AEM separated the cathodic and anodic compartments, each containing 1 M KOH aqueous electrolyte. For comparison, copper nanoparticles (Cu NPs) with comparable average diameters of ~25 nm were chosen and evaluated using the identical procedure (structural and morphological properties are presented in Supporting Information Figures S9–S11). Linear sweep voltammetry curves demonstrated that v-Cu NCs exhibited significantly larger current density with C_2H_2 compared to argon (Supporting Information Figures S12 and S13). Meanwhile, the converted v-Cu NCs displayed superior EHAE activity in comparison to commercial Cu NPs (Supporting Information Figure S14).[32] Steady-state chronoamperometric measurements were conducted for C_2H_2 electrolysis at various current densities, ranging from 0.1 to 1.1 A cm^{-2}. Gas chromatography was utilized for analysis and quantification of the reduced products at different current densities. Compared to Cu NPs, v-Cu NCs

Citation: *CCS Chem.* **2024**, Just Published. DOI: 10.31635/ccschem.024.202404849
Link to VoR: https://doi.org/10.31635/ccschem.024.202404849

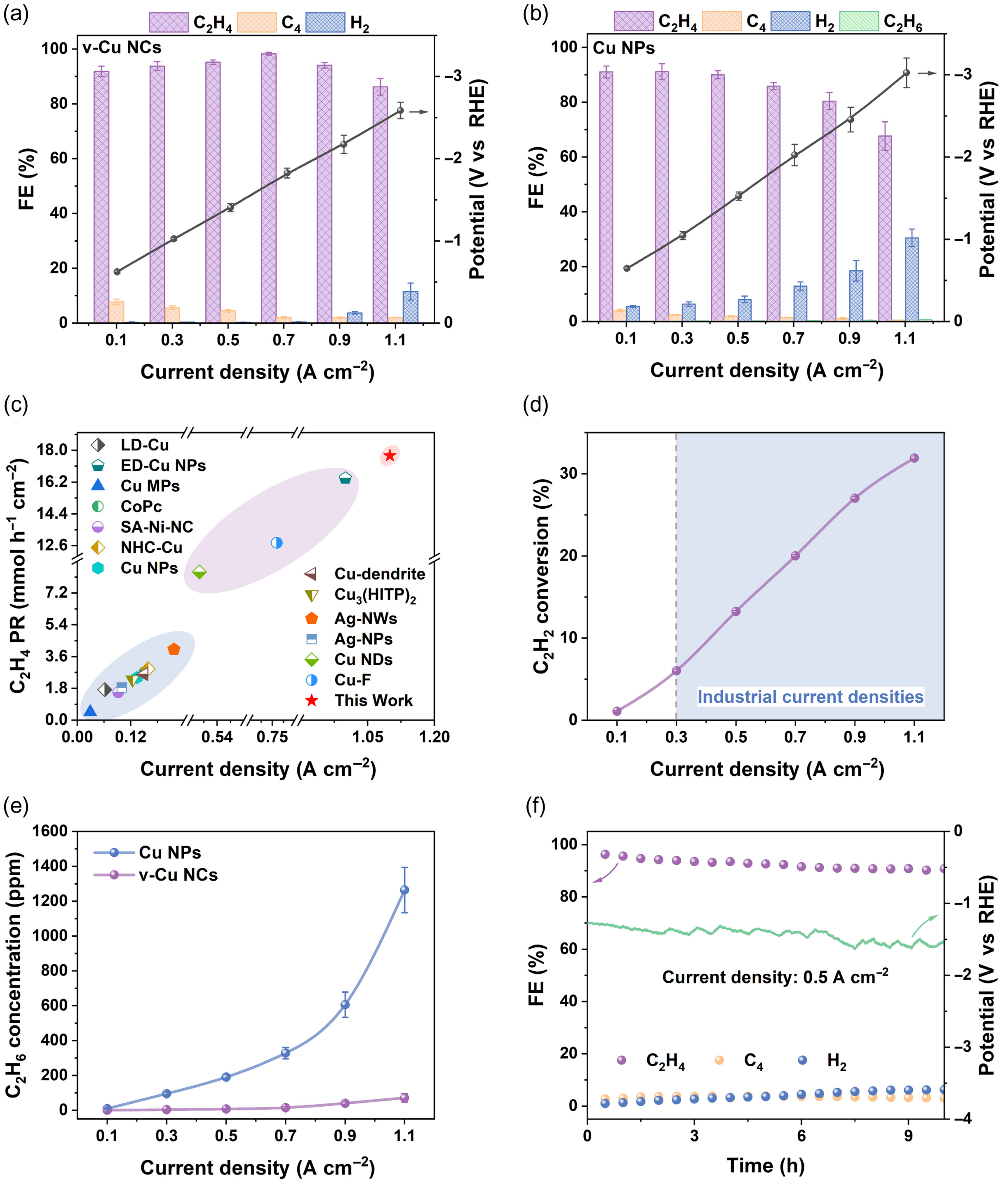

Figure 2 | *EHAE performance under pure C_2H_2 flow with 1 cm^2 electrolyzer. The FE of obtained products and corresponding potentials versus the applied current density on (a) v-Cu NCs and (b) Cu NPs. (c) Comparison of the C_2H_4 production rate of v-Cu NCs and the state-of-the-art reports. (d) The single-pass conversion rate of C_2H_2 and (e) the outlet C_2H_6 concentrations at different current densities. (f) Stability tests of v-Cu NCs for 10 h at 0.5 A cm^{-2} and C_2H_2 flow rate of 20 mL min^{-1}.*

showed a superior C_2H_4 production and reduced H_2 formation at all current densities (Figure 2a,b). In particular, the FE of C_2H_4 on v-Cu NCs reached up to 98.3% at 0.7 A cm^{-2} and maintained a high level of 94% even at 0.9 A cm^{-2} (Figure 2a). Moreover, the H_2 FE value was significantly reduced to 11.5% on v-Cu NCs from 30.5% on Cu NPs at a high current density of 1.1 A cm^{-2} (Supporting Information Figure S15). This resulted in a high C_2H_4 yield of 17.69 mmol h^{-1} cm^{-2} on v-Cu NCs (Supporting Information Figure S16), which outperformed most

Citation: *CCS Chem.* **2024**, Just Published. DOI: 10.31635/ccschem.024.202404849
Link to VoR: https://doi.org/10.31635/ccschem.024.202404849

reported electrocatalysts (Figure 2c, Supporting Information Figure S17 and Table S1).[2,3,6,7,11–14,17,33,34–36] Notably, the single-pass conversion rate of C_2H_2 was drastically elevated by the increase of current densities, and reaching 31.9% at 1.1 A cm^{-2} (Figure 2d). Additionally, the production of overhydrogenated C_2H_6 by-product exhibited a continuous increase with rising current densities on Cu NPs, from 9.4 ppm at 0.1 A cm^{-2} to 1264 ppm at 1.1 A cm^{-2}. In contrast, v-Cu NCs displayed a negligible amount of C_2H_6 (3 ppm at 0.3 A cm^{-2}), which slightly increased to 71 ppm at 1.1 A cm^{-2} (Figure 2e). Moreover, v-Cu NCs demonstrated exceptional stability over a duration of 10 h, maintaining an FE of C_2H_4 above 90% at a current density of 0.5 A cm^{-2} (Figure 2f).

Mechanism of the electrochemical semihydrogenation

To elucidate the origin of its superior activity and selectivity, a series of tests were conducted at different pH values to identify the generated H* species on v-Cu NCs. When the pH value shifted from neutral to alkaline, the increased C_2H_4 FE suggested that the EHAE process was more favorable under alkaline conditions (Supporting Information Figures S18 and S19) whereas, as the KOH concentration further increased, the C_2H_4 FE barely changed. Meanwhile, the significantly decreased potential indicated that a higher OH^- concentration favored the semihydrogenation of C_2H_2 (Supporting Information Figure S20). We can infer that the hydrogenation process occurring on v-Cu NCs deviates from the conventional electron-coupled proton transfer ($C_xH_y^* + H_2O + e^- \rightarrow C_xH_{y+1}^* + OH^-$, ECPT) route under high pH conditions.[3,6] Therefore, it is more plausible that $C_2H_2^*$ underwent hydrogenation through surface-adsorbed H*, which originated from water dissociation on v-Cu NCs.[3] This hypothesis found support in the slightly higher HER activity observed for v-Cu NCs compared to Cu NPs under an argon atmosphere (Supporting Information Figure S21). Similarly, a decrease in EHAE activity of v-Cu NCs was observed upon replacing 1 M KOH electrolyte with 1 M NaOH electrolyte (see Supporting Information Figures S22 and S23). This could be attributed to the smaller hydration radius and lower ionic hydration number of $K^+(H_2O)_n$ (n = 7 for K^+ and 13 for Na^+), facilitating the dissociation of water.[36,37] Quasi-in-situ EPR measurements were conducted under argon flows, and a distinct DMPO-H signal was observed after testing at −0.9 V versus RHE on both v-Cu NCs and Cu NPs (Figure 3a). Meanwhile, the intensity of the EPR spectrum for v-Cu NCs was stronger than that of Cu NPs at the same potential, indicating a higher ability for H* generation on v-Cu NCs.[2,38] However, despite the enhanced ability to dissociate water molecules, this did not result in increased HER on v-Cu NCs under C_2H_2 flow (Figure 2a,b). The exceptional catalytic activity of v-Cu NCs allowed for rapid consumption of generated H* for hydrogenation rather than its conversion into H_2.[3]

We further conducted in-situ Raman spectroscopy to identify the intermediates during the EHAE process (Figure 3b and Supporting Information Figure S24). The characteristic Raman peaks at 1350 and 1550 cm^{-1} corresponded to the D and G bands of carbon, respectively (Figure 3c).[39] The peak observed at 1693 cm^{-1} belonged to $C_2H_2^*$ intermediates adsorbed onto Cu sites.[14,32] With an increase in cathodic potential from 0 to −0.2 V versus RHE, two distinct peaks emerged at 1111 and 1502 cm^{-1} corresponding to the C–C and C=C bonds of polyacetylene, respectively. Meanwhile, a weaker peak at 1538 cm^{-1} referred to the weak π–d type adsorption of C_2H_4.[40,41] As the potential became more negative, the characteristic peaks of polyacetylene adsorbed on both v-Cu NCs and Cu NPs exhibited stronger intensities, indicating marked intensification of the EHAE process (Figure 3c and Supporting Information Figure S25). Notably, these peaks for $C_2H_2^*$ adsorption consistently presented on v-Cu NCs, whereas they gradually disappeared on Cu NPs with increasing potentials (Figure 3d). These results highlight that v-Cu NCs rapidly capture C_2H_2 at high current densities, allowing more C_2H_2 participation in the EHAE process. This prevents excessive coupling of H* into H_2 at active sites and ultimately leads to exceptional performance in C_2H_4 production.

The structural model of v-Cu (100) enriched with nitrogen vacancies was constructed to simulate the structure of v-Cu NCs for DFT calculations (Supporting Information Figure S26). To investigate the adsorption strength of C_2H_2, we calculated the projected density of states (PDOS) of Cu 3*d*-orbitals on v-Cu (100) and Cu (100). As shown in Figure 3e, the *d*-band center of v-Cu (100) is closer to the Fermi level compared to that of Cu (100), indicating a stronger adsorption strength for C_2H_2 on v-Cu (100) (Supporting Information Figures S27 and S28). The reaction free energy for the semihydrogenation of C_2H_2 to C_2H_4 on these Cu electrocatalysts is illustrated in Figure 3f and Supporting Information Table S2. The adsorption of C_2H_2 on Cu (100) is exothermic, leading to the formation of CH_2CH^* intermediates through hydrogenation of the adsorbed C_2H_2. Compared to Cu (100), v-Cu (100) exhibited enhanced adsorption affinities for intermediates, thereby facilitating H* adsorption on the electrocatalyst surface and promoting hydrogenation kinetics.[34]

It is well established that the energy barriers between $C_2H_4^* \rightarrow C_2H_4(g)$ (C_2H_4 desorption) and $C_2H_4^* + H^* \rightarrow C_2H_5^*$ (activation step) can provide straightforward evidence for the selectivity.[22,42] Specifically, Cu (100) and v-Cu (100) both showed higher energy barriers for the activation step than those of C_2H_4 desorption, indicating that $C_2H_4^*$ tended to desorb rather than undergo further hydrogenation (Figure 3g and Supporting Information Table S3). Meanwhile, the free energy difference

Citation: *CCS Chem.* **2024**, Just Published. DOI: 10.31635/ccschem.024.202404849
Link to VoR: https://doi.org/10.31635/ccschem.024.202404849

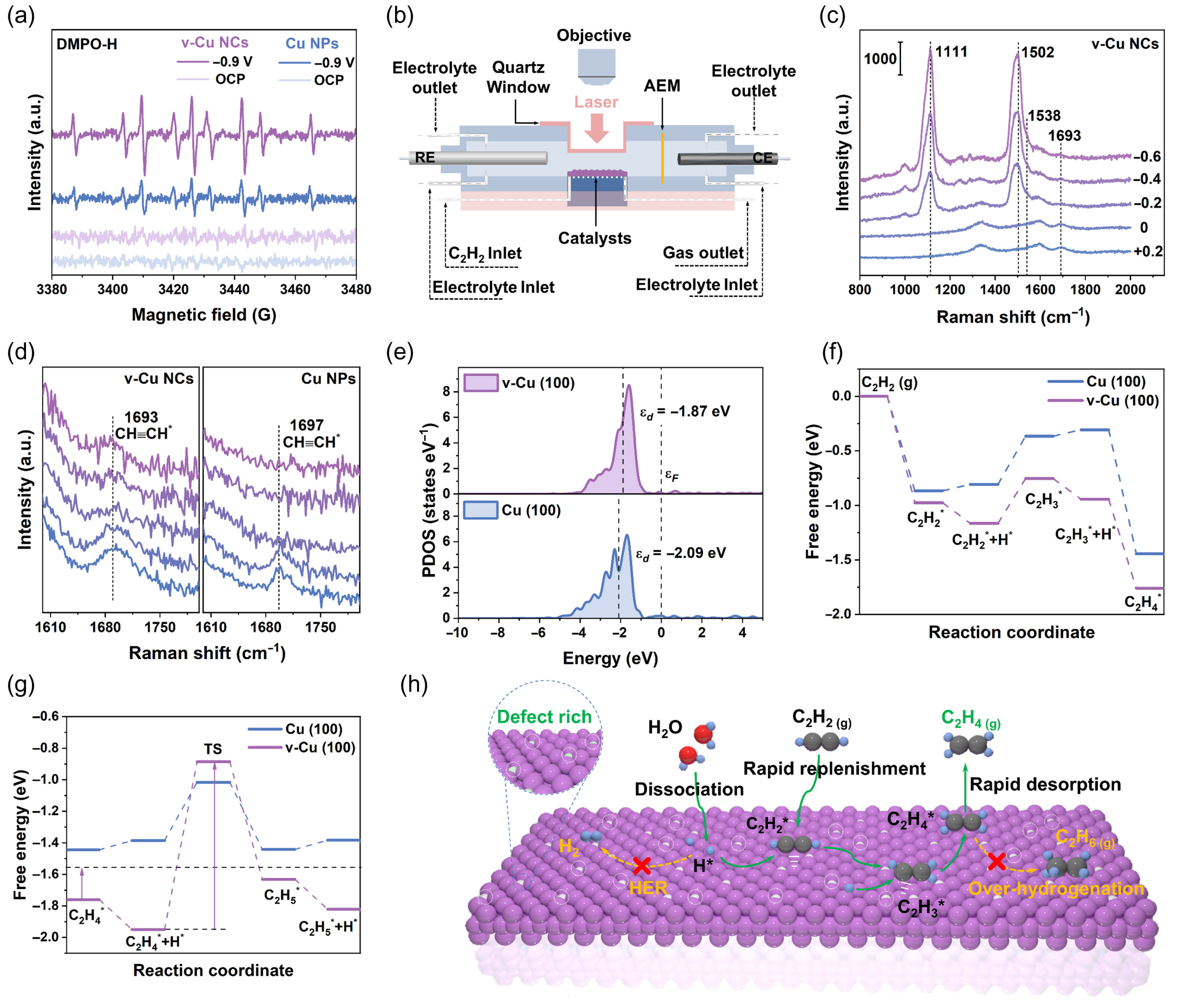

Figure 3 | *Mechanism investigations. (a) The quasi-in-situ EPR spectra for hydrogen radicals over v-Cu NCs and Cu NPs. (b) Schematic of the flow cell for in-situ electrochemical Raman test. (c) In-situ Raman spectra of v-Cu NCs and (d) a comparison of their EHAE performances. (e) The PDOS for v-Cu (100) and Cu (100). Free energy diagram for (f) the hydrogenation of C_2H_2 and (g) the C_2H_4 overhydrogenation reaction pathways on v-Cu (100) and Cu (100). (h) Schematic mechanism of EHAE process on v-Cu NCs.*

between C_2H_4 desorption and overhydrogenation (ΔG) on v-Cu (100) (0.86 eV) was higher than that of Cu (100) (0.49 eV), suggesting that the overhydrogenation process necessitated a higher energy input on v-Cu (100), thereby effectively suppressing overhydrogenation and enhancing selectivity for C_2H_4 production.

Based on these findings, we proposed a comprehensive mechanism of EHAE on v-Cu NCs (Figure 3h). Notably, the strong adsorption affinity of v-Cu NCs for C_2H_2 enabled continuous C_2H_2 supply during hydrogenation, resulting in superior EHAE performance at ultrahigh current densities while concurrently inhibiting competitive HER through rapid H* consumption. Additionally, the presence of defects significantly increased the energy barrier for converting C_2H_4* to C_2H_5* on v-Cu NCs, effectively inhibiting the overhydrogenation reaction.

Electrosynthesis of ethylene in a 25 cm^2 electrolyzer

To further enhance the single-pass conversion of C_2H_2, we assembled a 25 cm^2 electrolyzer (Supporting Information Figure S29).[2,14] The product distributions demonstrated an increased C_2H_2 single-pass conversion and C_2H_4 selectivity with rising cathode currents (Figure 4a). Notably, at the cathode current of 2 A, the

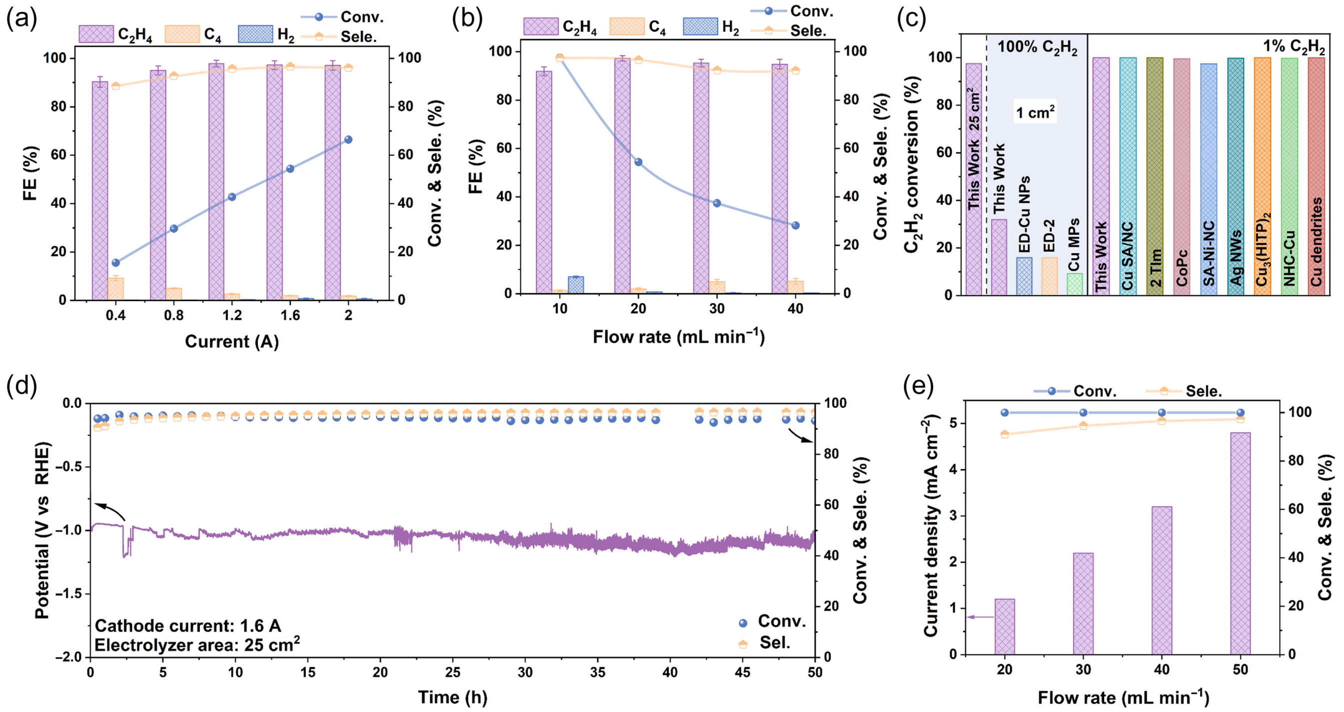

Figure 4 | *EHAE performance in a 25 cm^2 electrolyzer. FE distributions, C_2H_2 conversion, and selectivity of C_2H_4 (a) at different cathode currents in pure C_2H_2 flow (20 mL min^{-1}) and (b) at different flow rates with pure C_2H_2 feedstock. (c) Comparison of C_2H_2 conversion of v-Cu NCs with reported electrocatalysts. (d) The 50 h durability test of v-Cu NCs at 1.6 A with a pure C_2H_2 flow of 10 mL min^{-1}. (e) C_2H_2 conversion and selectivity of C_2H_4 at different flow rates using crude C_2H_4 containing 1% C_2H_2.*

FE and selectivity for C_2H_4 reached 97.1% and 96.1%, respectively, accompanied by an exceptional single-pass conversion of C_2H_2 reaching 66.4%. Moreover, HER and overhydrogenation reactions were effectively suppressed, resulting in an H_2 FE of only 0.65% and negligible amounts of C_2H_6 in the outlet (102 ppm). Moreover, the single-pass C_2H_2 conversion and C_2H_4 selectivity were measured at various flow rates (Figure 4b). At a gas flow rate of 10 mL min^{-1}, v-Cu NCs exhibited an impressive single-pass C_2H_2 conversion rate of 97.5% and C_2H_4 selectivity of 97.4% (Figure 4b). Notably, the record-high single-pass conversion rate of C_2H_2 was obtained in both 1 cm^2 (31.9%) and 25 cm^2 (97.5%) electrolyzers, which were even higher than those achieved by trace C_2H_2-removal electrocatalysts (Figure 4c and Supporting Information Table S4). Furthermore, no deterioration in the single-pass conversion of C_2H_2 and selectivity for C_2H_4 was observed on v-Cu NCs during the 50-hour stability test (Figure 4d). Additionally, we evaluated the performance of trace C_2H_2-removal using crude C_2H_4 containing 1% C_2H_2. Figure 4e exhibited that only a low current density (<5 mA cm^{-2}) was required for the efficient conversion of trace C_2H_2, achieving a high C_2H_2 conversion of 99.97% and a C_2H_4 specific selectivity of 97.2% (Supporting Information Figure S30).

Conclusion

In summary, the defect-rich v-Cu NCs electrocatalyst exhibited excellent EHAE reactivity and selectivity for converting C_2H_2 to C_2H_4. In-situ Raman spectroscopy and DFT calculations revealed that the abundance of defects endowed v-Cu NCs with the capability to rapidly and firmly capture C_2H_2 on Cu sites, accelerating the EHAE reaction kinetics, and inhibiting the competing HER. The higher activation energy barrier for C_2H_4 prevented its overhydrogenation, thereby hindering the formation of difficult-to-separate C_2H_6 by-product. Therefore, v-Cu NCs exhibited a remarkably high C_2H_4 FE of 98.3% at 0.7 A cm^{-2} and a production rate of 17.69 mmol h^{-1} cm^{-2} at 1.1 A cm^{-2}. Moreover, in a 25 cm^2 electrolyzer, we achieved the highest single-pass conversion rate of C_2H_2 at 97.5% with a flow rate of 10 mL min^{-1} of pure C_2H_2, while also maintaining a C_2H_4 selectivity of 97.4%.

Supporting Information

Supporting Information is available and includes additional experimental procedures and figures.

Conflict of Interest

There is no conflict of interest to report.

Funding Information

This work was supported by the National Natural Science Foundation of China (grant nos. 22322807, 22168023, 22268029, and 22108243), the Natural Science Foundation of Jiangxi Province (grant no. 20224ACB204003), the China Scholarship Council (grant no. 202206820025), and the Australian Research Council (ARC) through the ARC Discovery project (grant no. DP230101579).

Acknowledgments

The authors would like to thank the University of Technology-Sydney for the use of facilities within the Centre for Clean Energy Technology. Part of the experiment was carried out at the X-ray absorption spectroscopy beamline of the Australia National Synchrotron Radiation Research Centre.

References

1. Wang, Z.; Li, C.; Peng, G.; Shi, R.; Shang, L.; Zhang, T. Highly Selective Acetylene-to-Ethylene Electroreduction Over Cd-Decorated Cu Catalyst with Efficiently Inhibited Carbon-Carbon Coupling. *Angew. Chemie Int. Ed.* **2024**, *63*, e202400122.
2. Zhao, B.-H.; Chen, F.; Wang, M.; Cheng, C.; Wu, Y.; Liu, C.; Yu, Y.; Zhang, B. Economically Viable Electrocatalytic Ethylene Production with High Yield and Selectivity. *Nat. Sustain.* **2023**, *6*, 827–837.
3. Bai, L.; Wang, Y.; Han, Z.; Bai, J.; Leng, K.; Zheng, L.; Qu, Y.; Wu, Y. Efficient Industrial-Current-Density Acetylene to Polymer-Grade Ethylene via Hydrogen-Localization Transfer Over Fluorine-Modified Copper. *Nat. Commun.* **2023**, *14*, 8384.
4. Li, J.; Chen, Y.; Yao, B.; Yang, W.; Cui, X.; Liu, H.; Dai, S.; Xi, S.; Sun, Z.; Chen, W.; Qin, Y.; Wang, J.; He, Q.; Ling, C.; Wang, D.; Zhang, Z. Cascade Dual Sites Modulate Local CO Coverage and Hydrogen-Binding Strength to Boost CO_2 Electroreduction to Ethylene. *J. Am. Chem. Soc.* **2024**, *146*, 5693–5701.
5. Jiang, W.; Low, J.; Mao, K.; Duan, D.; Chen, S.; Liu, W.; Pao, C.-W.; Ma, J.; Sang, S.; Shu, C.; Zhan, X.; Qi, Z.; Zhang, H.; Liu, Z.; Wu, X.; Long, R.; Song, L.; Xiong, Y. Pd-Modified ZnO-Au Enabling Alkoxy Intermediates Formation and Dehydrogenation for Photocatalytic Conversion of Methane to Ethylene. *J. Am. Chem. Soc.* **2021**, *143*, 269–278.
6. Wang, S.; Uwakwe, K.; Yu, L.; Ye, J.; Zhu, Y.; Hu, J.; Chen, R.; Zhang, Z.; Zhou, Z.; Li, J.; Xie, Z.; Deng, D. Highly Efficient Ethylene Production via Electrocatalytic Hydrogenation of Acetylene Under Mild Conditions. *Nat. Commun.* **2021**, *12*, 7072.
7. Lv, X. H.; Huang, H.; Cui, L. T.; Zhou, Z. Y.; Wu, W.; Wang, Y. C.; Sun, S. G. Hydrogen Spillover Accelerates Electrocatalytic Semihydrogenation of Acetylene in Membrane Electrode Assembly Reactor. *ACS Appl. Mater. Interfaces* **2024**, *16*, 8668–8678.
8. Ma, J.; Su, B.; Wen, G.; Yang, Q.; Ren, Q.; Yang, Y.; Xing, H. Pyrolysis of Pulverized Coal to Acetylene in Magnetically Rotating Hydrogen Plasma Reactor. *Fuel Process. Technol.* **2017**, *167*, 721–729.
9. Liu, Z.; Zhang, L.; Ren, Z.; Zhang, J. Advances in Selective Electrocatalytic Hydrogenation of Alkynes to Alkenes. *Chem. Eur. J.* **2023**, *29*, e202202979.
10. Huang, L.; Bao, D.; Jiang, Y.; Zheng, Y.; Qiao, S. Electrocatalytic Acetylene Hydrogenation in Concentrated Seawater at Industrial Current Densities. *Angew. Chem. Int. Ed.* **2024**, *63*, e202405943.
11. Liu, Z.; Chen, Z.; Bu, J.; Ma, W.; Zhang, L.; Zhong, H.; Cheng, L.; Li, S.; Wang, T.; Zhang, J. Metal Phthalocyanines as Efficient Electrocatalysts for Acetylene Semihydrogenation. *Chem. Eng. J.* **2022**, *431*, 134129.
12. Ma, W.; Chen, Z.; Bu, J.; Liu, Z.; Li, J.; Yan, C.; Cheng, L.; Zhang, L.; Zhang, H.; Zhang, J.; Wang, T.; Zhang, J. π-Adsorption Promoted Electrocatalytic Acetylene Semihydrogenation on Single-Atom Ni Dispersed N-Doped Carbon. *J. Mater. Chem. A* **2022**, *10*, 6122–6128.
13. Li, J.; Guo, Y.; Chang, S.; Lin, J.; Wang, Y.; Liu, Z.; Wu, Y.; Zhang, J. Pairing D-Band Center of Metal Sites with π-Orbital of Alkynes for Efficient Electrocatalytic Alkyne Semi-Hydrogenation. *Small* **2023**, *19*, 2205845.
14. Bu, J.; Liu, Z.; Ma, W.; Zhang, L.; Wang, T.; Zhang, H.; Zhang, Q.; Feng, X.; Zhang, J. Selective Electrocatalytic Semihydrogenation of Acetylene Impurities for the Production of Polymer-Grade Ethylene. *Nat. Catal.* **2021**, *4*, 557–564.
15. Chen, Y.; Wu, Z.; Fan, L.; Krishna, R.; Huang, H.; Wang, Y.; Xiong, Q.; Li, J.; Li, L. Direct Ethylene Purification from Cracking Gas via a Metal-Organic Framework Through Pore Geometry Fitting. *Engineering* **2024**, *41*, 84–92.
16. Yang, R.; Wang, Y.; Cao, J.-W.; Ye, Z.-M.; Pham, T.; Forrest, K. A.; Krishna, R.; Chen, H.; Li, L.; Ling, B.-K.; Zhang, T.; Gao, T.; Jiang, X.; Xu, X.-O.; Ye, Q.-H.; Chen, K.-J. Hydrogen Bond Unlocking-Driven Pore Structure Control for Shifting Multi-Component Gas Separation Function. *Nat. Commun.* **2024**, *15*, 804.
17. Bai, R.; Li, J.; Lin, J.; Liu, Z.; Yan, C.; Zhang, L.; Zhang, J. Weak Acetylene Adsorption Terminated Carbon–Carbon Coupling Kinetics on Silver Electrocatalysts. *CCS Chem.* **2023**, *5*, 200–208.
18. Ge, X.; Dou, M.; Cao, Y.; Liu, X.; Yuwen, Q.; Zhang, J.; Qian, G.; Gong, X.; Zhou, X.; Chen, L.; Yuan, W.; Duan, X. Mechanism Driven Design of Trimer Ni_1Sb_2 Site Delivering Superior Hydrogenation Selectivity to Ethylene. *Nat. Commun.* **2022**, *13*, 5534.
19. Ball, M. R.; Rivera-Dones, K. R.; Gilcher, E. B.; Ausman, S. F.; Hullfish, C. W.; Lebrón, E. A.; Dumesic, J. A. AgPd and

Citation: *CCS Chem.* **2024**, Just Published. DOI: 10.31635/ccschem.024.202404849
Link to VoR: https://doi.org/10.31635/ccschem.024.202404849

CuPd Catalysts for Selective Hydrogenation of Acetylene. *ACS Catal.* **2020**, *10*, 8567–8581.

20. Jiang, X.; Tang, L.; Dong, L.; Sheng, X.; Zhang, W.; Liu, Z.; Shen, J.; Jiang, H.; Li, C. Cu Single-Atom Catalysts for High-Selectivity Electrocatalytic Acetylene Semihydrogenation. *Angew. Chem. Int. Ed.* **2023**, *135*, e202307848.

21. Chen, Z.; Cai, C.; Wang, T. Identification of Copper as an Ideal Catalyst for Electrochemical Alkyne Semi-Hydrogenation. *J. Phys. Chem. C* **2022**, *126*, 3037–3042.

22. Zhang, R.; Zhang, J.; Jiang, Z.; Wang, B.; Fan, M. The Cost-Effective Cu-Based Catalysts for the Efficient Removal of Acetylene from Ethylene: The Effects of Cu Valence State, Surface Structure and Surface Alloying on the Selectivity and Activity. *Chem. Eng. J.* **2018**, *351*, 732–746.

23. Parvizian, M.; Duràn Balsa, A.; Pokratath, R.; Kalha, C.; Lee, S.; Van den Eynden, D.; Ibáñez, M.; Regoutz, A.; De Roo, J. The Chemistry of Cu_3N and Cu_3PdN Nanocrystals. *Angew. Chem. Int. Ed.* **2022**, *61*, e202207013.

24. Guo, Q.; Liang, F.; Sun, Z.; Wang, Y.; Li, X.-B.; Xia, S.-G.; Zhang, Z. C.; Huang, L.; Wu, L.-Z. Optimal D-Band-Induced Cu_3N as a Cocatalyst on Metal Sulfides for Boosting Photocatalytic Hydrogen Evolution. *J. Mater. Chem. A* **2020**, *8*, 22601–22606.

25. Yin, Z.; Yu, C.; Zhao, Z.; Guo, X.; Shen, M.; Li, N.; Muzzio, M.; Li, J.; Liu, H.; Lin, H.; Yin, J.; Lu, G.; Su, D.; Sun, S. Cu_3N Nanocubes for Selective Electrochemical Reduction of CO_2 to Ethylene. *Nano Lett.* **2019**, *19*, 8658–8663.

26. Peng, C.; Luo, G.; Xu, Z.; Yan, S.; Zhang, J.; Chen, M.; Qian, L.; Wei, W.; Han, Q.; Zheng, G. Lithiation-Enabled High-Density Nitrogen Vacancies Electrocatalyze CO_2 to C_2 Products. *Adv. Mater.* **2021**, *33*, 2103150.

27. Zhao, C.; Luo, G.; Liu, X.; Zhang, W.; Li, Z.; Xu, Q.; Zhang, Q.; Wang, H.; Li, D.; Zhou, F.; Qu, Y.; Han, X.; Zhu, Z.; Wu, G.; Wang, J.; Zhu, J.; Yao, T.; Li, Y.; Bouwmeester, H. J. M.; Wu, Y. In Situ Topotactic Transformation of an Interstitial Alloy for CO Electroreduction. *Adv. Mater.* **2020**, *32*, 2002382.

28. Zhang, Z.; Chen, S.; Zhu, J.; Ye, C.; Mao, Y.; Wang, B.; Zhou, G.; Mai, L.; Wang, Z.; Liu, X.; Wang, D. Charge-Separated $Pd^{\delta-}$-$Cu^{\delta+}$ Atom Pairs Promote CO_2 Reduction to C_2. *Nano Lett.* **2023**, *23*, 2312–2320.

29. Zhang, B.; Dai, Z.; Chen, Y.; Cheng, M.; Zhang, H.; Feng, P.; Ke, B.; Zhang, Y.; Zhang, G. Defect-Induced Triple Synergistic Modulation in Copper for Superior Electrochemical Ammonia Production Across Broad Nitrate Concentrations. *Nat. Commun.* **2024**, *15*, 2816.

30. Luc, W.; Fu, X.; Shi, J.; Lv, J.-J.; Jouny, M.; Ko, B. H.; Xu, Y.; Tu, Q.; Hu, X.; Wu, J.; Yue, Q.; Liu, Y.; Jiao, F.; Kang, Y. Two-Dimensional Copper Nanosheets for Electrochemical Reduction of Carbon Monoxide to Acetate. *Nat. Catal.* **2019**, *2*, 423–430.

31. Zhang, Z.; Feng, X.; Zhang, Z.; Chen, L.; Liu, W.; Tong, L.; Gao, X.; Zhang, J. Graphdiyne Enabled Nitrogen Vacancy Formation in Copper Nitride for Efficient Ammonia Synthesis. *J. Am. Chem. Soc.* **2024**, *146*, 14898–14904.

32. Xue, W.; Liu, X.; Liu, C.; Zhang, X.; Li, J.; Yang, Z.; Cui, P.; Peng, H.-J.; Jiang, Q.; Li, H.; Xu, P.; Zheng, T.; Xia, C.; Zeng, J. Electrosynthesis of Polymer-Grade Ethylene via Acetylene Semihydrogenation Over Undercoordinated Cu Nanodots. *Nat. Commun.* **2023**, *14*, 2137.

33. Zhang, L.; Chen, Z.; Liu, Z.; Bu, J.; Ma, W.; Yan, C.; Bai, R.; Lin, J.; Zhang, Q.; Liu, J.; Wang, T.; Zhang, J. Efficient Electrocatalytic Acetylene Semihydrogenation by Electron-Rich Metal Sites in *N*-Heterocyclic Carbene Metal Complexes. *Nat. Commun.* **2021**, *12*, 6574.

34. Shi, R.; Wang, Z.; Zhao, Y.; Waterhouse, G. I. N.; Li, Z.; Zhang, B.; Sun, Z.; Xia, C.; Wang, H.; Zhang, T. Room-Temperature Electrochemical Acetylene Reduction to Ethylene with High Conversion and Selectivity. *Nat. Catal.* **2021**, *4*, 565–574.

35. Chang, S.; Bu, J.; Li, J.; Lin, J.; Liu, Z.; Ma, W.; Zhang, J. Highly Efficient Electrocatalytic Deuteration of Acetylene to Deuterated Ethylene Using Deuterium Oxide. *Chinese Chem. Lett.* **2023**, *34*, 107765.

36. Wu, Y.; Liu, C.; Wang, C.; Yu, Y.; Shi, Y.; Zhang, B. Converting Copper Sulfide to Copper with Surface Sulfur for Electrocatalytic Alkyne Semihydrogenation with Water. *Nat. Commun.* **2021**, *12*, 3881.

37. Gao, Y.; Yang, R.; Wang, C.; Liu, C.; Wu, Y.; Li, H.; Zhang, B. Field-Induced Reagent Concentration and Sulfur Adsorption Enable Efficient Electrocatalytic Semihydrogenation of Alkynes. *Sci. Adv.* **2022**, *8*, eabm9477.

38. Cao, X.; Ding, Y.; Chen, D.; Ye, W.; Yang, W.; Sun, L. Cluster-Level Heterostructure of PMo_{12}/Cu for Efficient and Selective Electrocatalytic Hydrogenation of High-Concentration 5-Hydroxymethylfurfural. *J. Am. Chem. Soc.* **2024**, *146*, 25125–25136.

39. Gong, S.; Wang, W.; Zhang, C.; Zhu, M.; Lu, R.; Ye, J.; Yang, H.; Wu, C.; Liu, J.; Rao, D.; Shao, S.; Lv, X. Tuning the Metal Electronic Structure of Anchored Cobalt Phthalocyanine via Dual-Regulator for Efficient CO_2 Electroreduction and Zn–CO_2 Batteries. *Adv. Funct. Mater.* **2022**, *32*, 2110649.

40. Lefrant, S.; Lichtmann, L. S.; Temkin, H.; Fitchen, D. B.; Miller, D. C.; Whitwell, G. E.; Burlitch, J. M. Raman Scattering in $(CH)_x$ and $(CH)_x$ Treated with Bromine and Iodine. *Solid State Commun.* **1979**, *29*, 191–196.

41. Patterson, M. L.; Weaver, M. J. Surface-Enhanced Raman Spectroscopy as a Probe of Adsorbate-Surface Bonding: Simple Alkenes and Alkynes Adsorbed at Gold Electrodes. *J. Phys. Chem.* **1985**, *89*, 5046–5051.

42. Zhang, R.; Zhang, J.; Zhao, B.; He, L.; Wang, A.; Wang, B. Insight into the Effects of Cu Component and the Promoter on the Selectivity and Activity for Efficient Removal of Acetylene from Ethylene on Cu-Based Catalyst. *J. Phys. Chem. C* **2017**, *121*, 27936–27949.

Citation: *CCS Chem.* **2024**, Just Published. DOI: 10.31635/ccschem.024.202404849
Link to VoR: https://doi.org/10.31635/ccschem.024.202404849